PAPER

Heterojunctions of halogen-doped carbon nitride nanosheets and BiOI for sunlight-driven water-splitting

To cite this article: Kazi M Alam *et al* 2020 *Nanotechnology* **31** 084001

View the article online for updates and enhancements.

IOP ebooks™

Bringing you innovative digital publishing with leading voices to create your essential collection of books in STEM research.

Start exploring the collection - download the first chapter of every title for free.

Heterojunctions of halogen-doped carbon nitride nanosheets and BiOI for sunlight-driven water-splitting

Kazi M Alam[1,3]**, Pawan Kumar**[1,3] ⬤**, Piyush Kar**[1]**, Ankur Goswami**[1]**,
Ujwal K Thakur**[1]**, Sheng Zeng**[1]**, Ehsan Vahidzadeh**[1]**, Kai Cui**[2] **and
Karthik Shankar**[1] ⬤

[1] Department of Electrical & Computer Engineering, University of Alberta, Edmonton, Alberta T6G 1H9,
Canada
[2] Nanotechnology Research Centre, National Research Council of Canada, Edmonton, Alberta, Canada

E-mail: kshankar@ualberta.ca

Abstract

A fluorine-doped, chlorine-intercalated carbon nitride (CNF-Cl) photocatalyst has been synthesized for simultaneous improvements in light harvesting capability along with suppression of charge recombination in bulk g-C_3N_4. The formation of heterojunctions of these CNF-Cl nanosheets with low bandgap, earth abundant bismuth oxyiodide (BiOI) was achieved, and the synthesized heterojunctions were tested as active photoanodes in photoelectrochemical water splitting experiments. BiOI/CNF-Cl heterojunctions exhibited extended light harvesting with a band-edge of 680 nm and generated photocurrent densities approaching 1.3 mA cm^{-2} under AM1.5 G one sun illumination. Scanning Kelvin probe force microscopy under optical bias showed a surface potential of 207 mV for the 50% BiOI/CNF-Cl nanocomposite, while pristine CNF-Cl and BiOI had surface photopotential values of 83 mV and 98 mV, respectively, which in turn, provided direct evidence of superior charge separation in the heterojunction blends. Enhanced charge carrier separation and improved light harvesting capability in BiOI/CNF-Cl hybrids were found to be the dominant factors in increased photocurrent, compared to the pristine constituent materials.

Supplementary material for this article is available online

Keywords: graphenic semiconductors, 2D materials, bismuth oxyhalides, photophysics, charge carrier recombination

(Some figures may appear in colour only in the online journal)

1. Introduction

Photocatalysis technology has the potential to address both steadily rising global energy demand and environmental pollution issues [1]. Water-splitting photoelectrochemical cells (PECs) have several advantages over other renewable energy device technologies since a PEC harvests plentiful and inexhaustible solar energy and converts water into hydrogen, which is a portable, high energy density fuel. The performance of a photoelectrocatalyst depends on several aspects of a complex process, such as band positions, light harvesting, charge excitation, charge separation, charge transfer and surface electrocatalytic reactions [2]. Therefore the overall efficiency is a function of the efficiencies of all these individual steps, a fact that has motivated a search for ideal photocatalytic systems with optimized electronic band-gaps, facile charge separation, adequate carrier transport, morphologies and dimensions comparable to carrier diffusion lengths, high density of active surface sites, etc. Several oxide/sulfide based semiconductors such as TiO_2, ZnS, CdS,

---

[3] These authors contributed equally.

ZnO, BiVO$_4$, and complex composition materials i.e. La- and Rh-codoped SrTiO$_3$ (SrTiO$_3$:La, Rh) have been explored as photoanodes for water splitting. However, no photoelectrocatalyst has achieved a satisfactory performance for the deployment of PEC technology at an industrial scale [3, 4].

Graphitic carbon nitride (g-C$_3$N$_4$), a metal-free two-dimensional conjugated semiconducting polymer, composed of tris-*s*-triazine (C$_6$N$_7$) units linked together with tertiary nitrogen is currently being intensely studied for the realization of efficient artificial photosynthetic systems [2, 5–14]. g-C$_3$N$_4$ and related graphenic frameworks are particularly promising for PECs because of the following reasons: (i) They are constituted of earth abundant elements (carbon and nitrogen) (ii) They have relatively simple, scalable and inexpensive methods of synthesis (iii) g-C$_3$N$_4$ has a moderate bandgap (2.7 eV) with suitable band-edge positions (Ecb: -1.1 V and Evb: $+1.6$ V versus NHE at pH-0) for water-splitting and (iv) They possesses good thermal stability (stable up to 600 °C), photochemical stability (non-photocorrosive) and chemical stability (resistant to strong acids and bases) [2, 6, 7, 9, 15]. Despite these attractive features, g-C$_3$N$_4$ suffers from fast charge carrier recombination and narrow visible light absorption limited to the blue region of the solar spectrum [14]. Many attempts have been made to improve the light absorption capability, such as surface area modification, doping with P, N, F, I, Cl, B etc and incorporation of N-rich units in cross-linked heptazine framework [16–21]. The synthesis of F-doped carbon nitride using ammonium fluoride (NH$_4$F) as a dopant material revealed that F atoms are bonded to C atoms in the corners and bays through transformation of sp^2 C to sp^3 C [22]. This shifts the highest occupied molecular orbital (HOMO) and lowest unoccupied molecular orbital (LUMO) positions and results in a reduced bandgap and enhanced photocatalytic performance [22]. Bulk g-C$_3$N$_4$ possesses hydrogen bonding between graphitic sheets, which remains a potential source of localized interlayer charge recombination, detrimental to photocatalytic activity. Therefore, few-layered or single-layered crystalline sheets (with periodic heptazine units) are highly desirable to realize better charge separation through the suppression of inter-layer charge recombination [23–25]. Several attempts have been made to transform bulk g-C$_3$N$_4$ into few-layered or single-layered nanosheets namely, solvent exfoliation, oxidation, varying precursors, etc [26–29]. In this regard, using sheets-forming-precursor is most attractive as it precludes hazardous chemicals involved in chemical exfoliation [30, 31]. Lu *et al* demonstrated the use of ammonium chloride (NH$_4$Cl) with dicyandiamide; the carbon nitride precursor released NH$_3$ and HCl gases during thermal annealing which blew dicyandiamide derived polymers into numerous large bubbles, which behaved as gas templates and yielded few-layered g-C$_3$N$_4$ nanosheets [30]. In another report Liu *et al* showed that NH$_4$Cl not only assisted in the transformation into sheets but excess NH$_4$Cl also facilitated chlorine intercalation in between g-C$_3$N$_4$ sheets which acted as a charge transport gallery to reduce the recombination rate and improved the porous structure [19]. Motivated by these findings, we have demonstrated the synthesis of few-layered fluorine-doped and chlorine-intercalated carbon nitride nanosheets (CNF-Cl) using dicyandiamide as a precursor for carbon nitride skeleton while NH$_4$F and NH$_4$Cl were used as sources for F and Cl (sheets determining agent), respectively.

Recently, earth abundant ternary compound semiconductors from the bismuth oxyhalide (BiOX, X=Cl, Br, I) family have received significant attention for their high photocatalytic activities owing to small bandgaps (1.7–1.9 eV) and suitable nanomorphology. Narrow bandgap BiOI possesses a layered crystal structure in which positive [Bi$_2$O$_2$]$^{2+}$ layers are interleaved with negatively charged iodide slabs [32–36]. This creates an internal built-in electric field which facilitates the separation and transport of photogenerated electron–hole pairs [37–41]. Another attractive feature of the BiOI band structure lies in its dispersive nature, which enables excitation of electrons through multiple pathways [40]. Despite the above mentioned attributes, BiOI remains a poor photocatalyst due to many unwanted features such as low conductivity, fast charge recombination, etc [38, 40]. The key scientific challenge therefore is to achieve a much higher photocatalytic and/or photoelectrochemical performance using BIOI-based platforms. Recently, certain research groups have reported the photocatalytic performances of BiOI-based type-II heterostructures [42–49]. In this work, we have attempted to suppress interlayer charge recombination of bulk carbon nitride by two efficient, facile and cost-effective steps, namely (1) formation of few-layered fluorine-doped and chlorine-intercalated nanosheets (CNF-Cl) and (2) *in situ* growth of heterojunctions of CNF-Cl with BiOI. The resulting BiOI/CNF-Cl heterojunctions showed remarkable improvement in the measured photocurrent densities under AM1.5 G one sun illumination. BiOI/CNF-Cl demonstrated excellent photoelectrochemical H$_2$ evolution rate (19.71 μmol h^{-1}) and Faradaic efficiency (82.83%) in comparison to pristine BiOI and CNFCl. The superior performance of the nanocomposite catalysts is attributed to the enhanced charge separation and improved light harvesting capability.

2. Results and discussion

2.1. Synthesis, morphological, structural and compositional analysis

The synthesis of few-layered F doped Cl-intercalated carbon nitride (CNF-Cl) sheets was pursued by thermal annealing of dicyandiamide, NH$_4$F and NH$_4$Cl at 550 °C through a slight modification of previous reported methods (figure 1) [19, 22, 30]. In this synthesis protocol dicyandiamide serves as the source of carbon and nitrogen. High temperature condensation polymerization of dicyandiamide yields heptazine (C$_6$N$_7$) units containing g-C$_3$N$_4$ framework via melamine, melon, melem, intermediates and evolution of ammonia. NH$_4$F facilitates fluorine doping of heptazine moieties because of degradation of NH$_4$F during thermal annealing and released F atom make bonds to heptazine ring carbons. The incorporation of electron withdrawing F atoms in g-C$_3$N$_4$ scaffold transforms some sp^2 hybridized C atoms in to sp^3 C
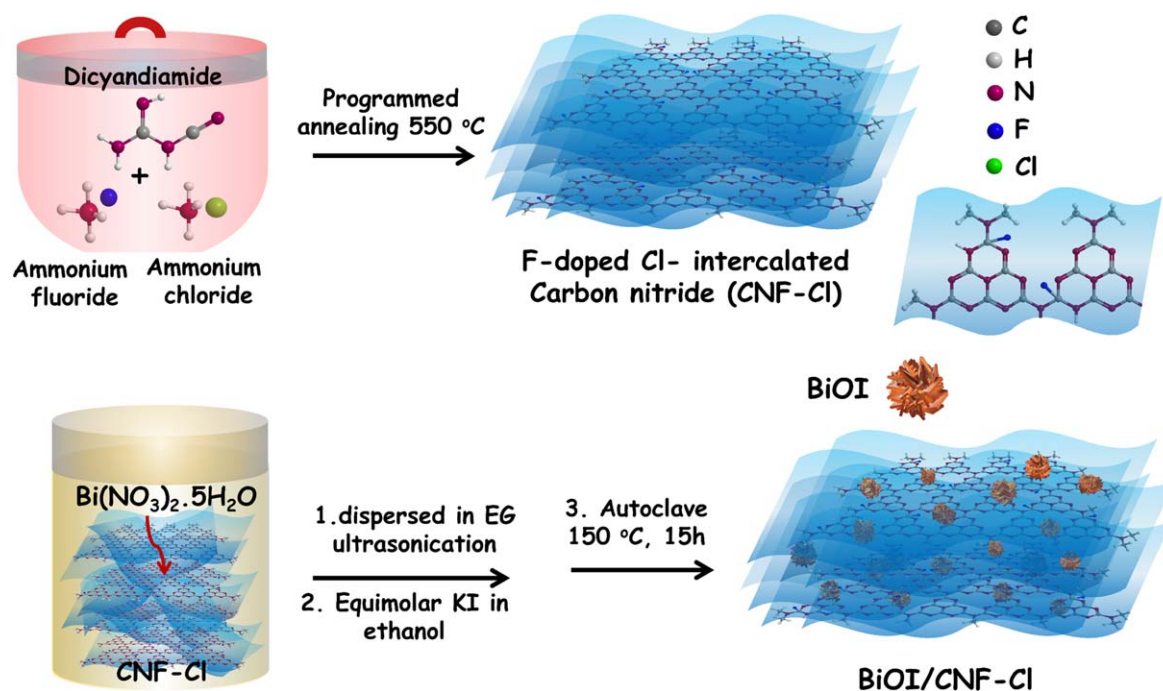
Figure 1. Synthetic outline for the preparation of F doped Cl-intercalated g-C$_3$N$_4$ (CNF-Cl) and BiOI/CNF-Cl nanostructured heterojunction.

which partially distorted in-plane symmetry of conjugated network resulting in the shifting of HOMO and LUMO positions (band edge positions) and a reduction of the bandgap [22]. NH$_4$Cl plays a dual role in the synthesis- (1) facilitating the formation of few-layered sheets due to release of NH$_3$ and HCl gases at elevated temperature that blow dicyandiamide-derived polymers into numerous large bubbles, yielding F doped g-C$_3$N$_4$ nanosheets [30] and (2) chlorine intercalation in between g-C$_3$N$_4$ layers. The chlorine intercalation in between few-layered F-doped carbon nitride sheets provides interlayer galleries for better charge migration along with uplifting of the conduction band and a narrower bandgap [19]. The detailed experimental protocols and physicochemical characterization methodologies i.e. Fourier transform infrared spectroscopy, electrochemical impedance spectroscopy (EIS) and Mott–Schottky plots, efficiency calculations (ABPE, IPCE, APCE and Faradaic efficiency) and reuse experiment results are provided in supporting information.

The fine morphological attributes of BiOI/CNFCl composite to discern the presence of CNF-Cl sheets and dendritic BiOI nanoplates were determined using high-resolution transmission electron microscopy (HR-TEM). The HR-TEM image of BiOI/CNF-Cl clearly shows dense and more crystalline domains correspond to BiOI while less dense domains indicate CNF-Cl in the heterostructure (figures 2(a)–(c)). High magnification HRTEM image displayed lattice fringes of CNF-Cl and BiOI with interplanar *d*-spacing of 0.32 and 0.28 nm assigned to (002) plane of CNF-Cl and (110) plane of BiOI, respectively (figures 2(b), (c)) [45, 50]. The obtained *d*-spacings were in excellent agreement with XRD results (figure 3(a)). The presence of (002) plane specific to graphitic structure suggests CNF-Cl sheets were stacked together in the

BiOI/CNF-Cl nanocomposites. The overlapping of these materials onto each other is unambiguously evident in figure 2(b), where both the crystal lattices are identified in the same region. Figure 2(e) shows the FESEM image of BiOI/CNF-Cl composite, where both stacked layers comprising the two materials are visible, in agreement with the TEM images. A closer observation reveals the hydrothermally synthesized dendritic BiOI nanoplates scaffolded with CNF-Cl framework. Elemental mapping BiOI/CNF-Cl heterojunction in scanning transmission electron microscopy mode clearly showed even distribution of the Bi, I and O in dense region and C, N and F in both less dense and dense regions (figures 2(f)–(l), respectively). Due to the partial overlap of Bi and Cl peaks, pristine CNF-Cl was also mapped which clearly demonstrates the presence of Cl in nanosheets [51]. Figures 2(m)–(q) show the constituent elements of CNF-Cl, C, N, F and Cl, respectively.

The XRD spectra of CNF-Cl exhibited a broad peak centered at ~27.1° corresponding to the (002) plane which indicates interlayer stacking of conjugated aromatic sheets, with a 0.33 nm interlayer *d* spacing, while the other small peak at 13.1° corresponding to the (100) reflection represents in-plane repetition of tri-*s*-triazine unit, consistent with previously reported data for g-C$_3$N$_4$ (figure 3(a)) [13, 52]. This *d* spacing was slightly higher than reported for pristine g-C$_3$N$_4$ (0.32 nm), which might be due to the increased repulsion between sheets caused by out-of-plane F atoms [53]. The XRD plot for pristine BiOI demonstrated all the peaks associated with tetragonal phase of BiOI which was in good agreement with reported literature [43, 54]. As expected, the XRD peak intensities of BiOI decrease, while these intensities increase for CNF-Cl with the increase of CNF-Cl wt% in the BiOI/CNF-Cl composites. The appearance of both (002) and
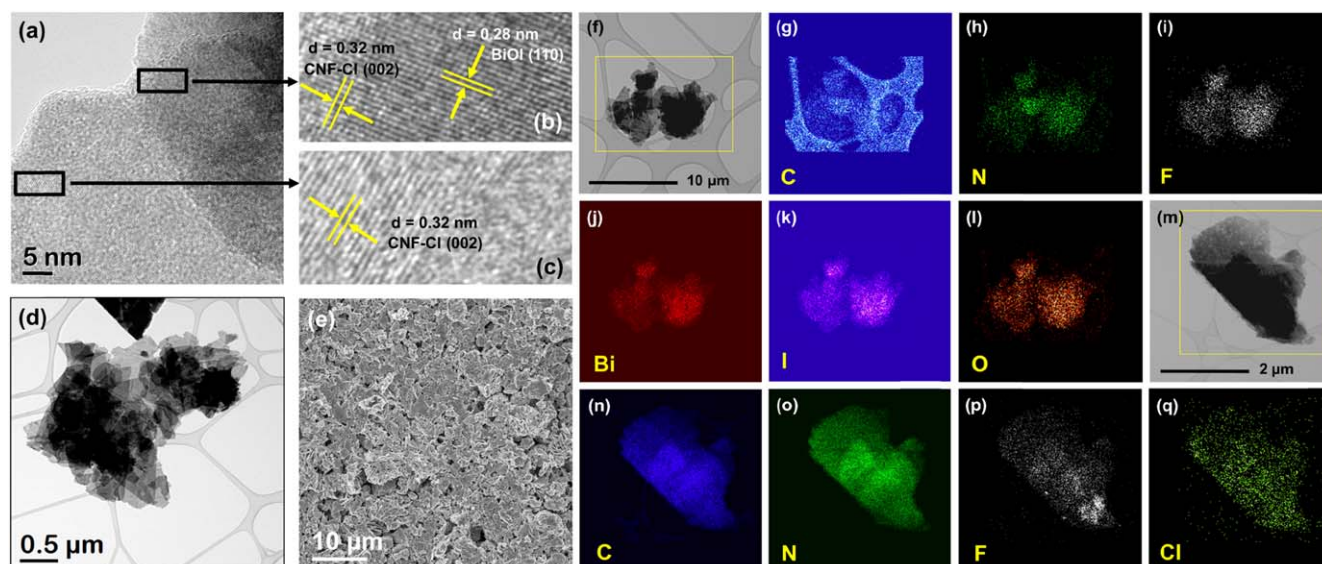
Figure 2. (a) HRTEM image of 50% BiOI/CNF-Cl; (b) and (c) selected magnified regions of (a) showing crystal planes of CNF-Cl and BiOI; (d) bright field STEM image of 50% BiOI/CNF-Cl; (e) FESEM image of 50% BiOI/CNF-Cl film, (f) and (m) bright field STEM images of 50% BiOI/CNF-Cl and pristine CNF-Cl, respectively; (g)–(l) EDX elemental mapping of 50% BiOI/CNF-Cl under STEM mode for C (g), N (h), F (i), Bi (j), I (k) and O (l); (n)–(q) EDX elemental mapping of pristine CNF-Cl under STEM mode for C (n), N (o), F (p), and Cl (q).
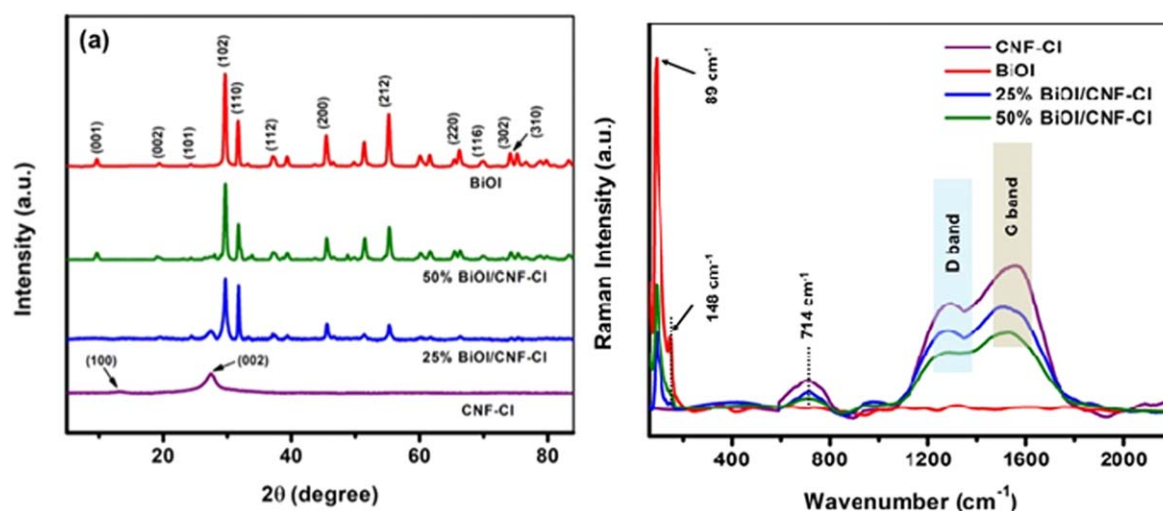

Figure 3. (a) X-ray diffractograms of pristine BiOI, BiOI/CNF-Cl composites and pristine CNF-Cl and (b) Raman spectra ($\lambda_{exc} = 785$ nm) of pristine CNF-Cl, pristine BiOI and BiOI/CNF-Cl heterostructures.

(100) peaks of CNF-Cl in the composite heterostructures, confirms the presence of CNF-Cl with preserved graphitic carbon nitride framework.

Figure 3(b) shows the Raman spectra for pristine CNF-Cl, BiOI and BiOI/CNF-Cl the heterostructures. Two characteristic peaks in between 1300 and 1600 cm^{-1} assigned to D and G bands of graphene-based materials were clearly visible in the Raman spectra of the pristine CNF-Cl and their composites with BiOI. The D band is associated with the out of plane vibrations of sp^3 carbon atoms, representative of defects and disorder in the systems, and the G band is assigned to E_{2g} phonons at Γ point, which originates from the in-plane vibrations of sp^2 carbon atoms [55, 56]. Unlike graphene or graphene oxide based materials, carbon nitride based materials do not exhibit sharp D and G bands due to

plenty of defects and short range ordered structure. The relative intensities of the Raman peaks corresponding to the D and G bands, provide an indication of defects and order in carbon nitride materials. In pristine bulk g-C$_3$N$_4$, $I_D/I_G = 0.36$, which increases to 0.82 in fluorinated g-C$_3$N$_4$ due to increased disorder [57]. In both pristine CNF-Cl and the CNF-Cl containing composites prepared by us, the ratio $I_D/I_G \sim 0.74$, close to that of fluorinated g-C$_3$N$_4$. The almost unchanged intensity ratio (I_D/I_G) of these bands, in the BiOI/CNF-Cl nanocomposites, compared to the pristine CNF-Cl is indicative of unperturbed crystallinity, order and in-plane sp^2 domain size in the nanocomposites, consistent with the XRD results. The relatively smaller peak around 714 cm^{-1}, which has been attributed to the out of plane C–C vibrations [58], is present in the spectrum of both pristine CNF-Cl and
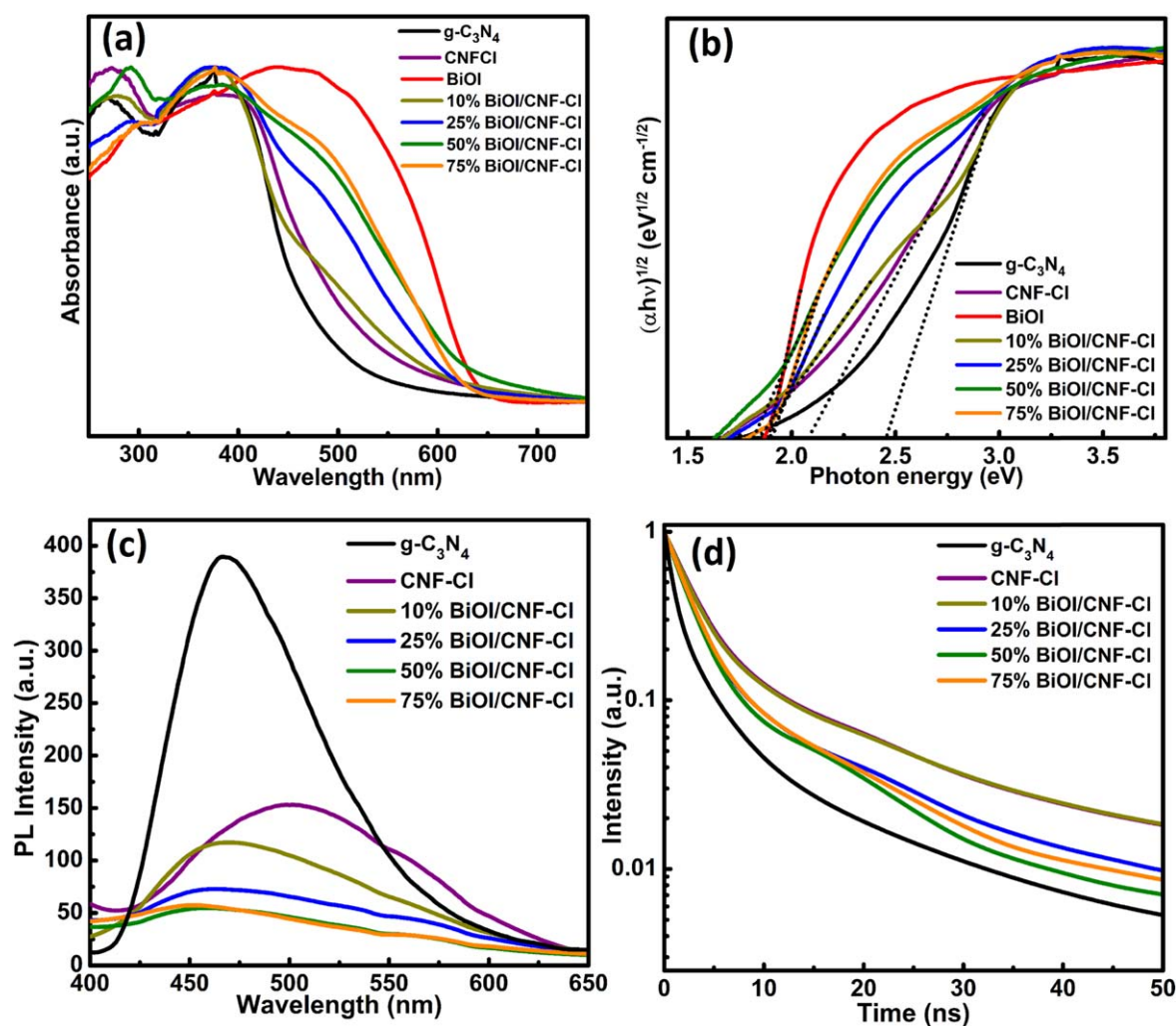
Figure 4. (a) UV–vis absorption spectra collected in diffuse reflectance spectroscopy (DRS) mode and (b) Tauc plots for the determination of the effective optical bandgaps of pristine g-C_3N_4, pristine CNF-Cl, pristine BiOI and BiOI/CNF-Cl heterostructures. (c) Steady state photoluminescence spectra ($\lambda_{exc} = 360$ nm) and (d) time resolved photoluminescence spectra ($\lambda_{exc} = 405$ nm) for conventional g-C_3N_4, pristine CNF-Cl and BiOI/ CNF-Cl heterostructures.

BiOI/CNF-Cl heterostructures. The sharp Raman peaks at the lower wavenumbers are vibrational modes of BiOI. The peak at $148\,\mathrm{cm}^{-1}$ is assigned to the E_g internal Bi–I stretching mode [59]. As expected, the relative intensities of the D and G bands of CNF-Cl decreased in BiOI/CNF-Cl composite as the wt% of BiOI increased.

2.2. Photophysical properties

Prior to the photocatalytic testing experiments, we studied the photophysical properties of conventional bulk g-C_3N_4, as-prepared CNF-Cl, pristine BiOI, and BiOI/CNF-Cl nano-composites using UV–vis spectroscopy (collected in diffuse reflectance mode), steady state photoluminescence (SSPL) spectroscopy and time resolved photoluminescence (TRPL). Figure 4a shows the UV–vis absorption spectra of these materials. CNF-Cl shows an absorption band ∼270 nm due to $\pi \to \pi^*$ transition that originates from the two-coordinated nitrogen vacancy in the conjugated ring, while another band around 380 nm with band tail extended up to 500 nm, is believed to originate from the $n \to \pi^*$ transition, associated

with N lone pair (LP) electrons in triazine/heptazine rings [60, 61]. The fluorine doping and chlorine intercalation in CNF-Cl improves visible harvesting over conventional g-C_3N_4 by generating a ca. 50 nm redshift in the optical absorption. Despite the red-shifted absorption, the bandgap of pristine CNF-Cl is still relatively large, while the composite heterojunction with a small bandgap material, such as BiOI improves the light harvesting capability to a significant extent. Pristine BiOI exhibits a band-edge at ∼680 nm. Two clear band edges, corresponding to CNF-Cl and BiOI, can be seen from the plots of nanocomposite heterostructures (figure 4(a)). Further, bandgaps of the as-prepared materials were estimated using Tauc plots (figure 4(b)) through extra-polation of the linear regions of graphs between $(\alpha h\nu)^{1/2}$ versus $h\nu$ on abscissa where α is the absorption coefficient, h is Planck's constant and ν is the frequency of light. The effective bandgaps of g-C_3N_4, pristine CNF-Cl, pristine BiOI, 10% BiOI/CNF-Cl, 25% BiOI/CNF-Cl, 50% BiOI/CNF-Cl and 75% BiOI/CNF-Cl were found to be 2.46, 2.05 eV, 1.88 eV, 1.86 eV, 1.88 eV, 1.81 eV and 1.88 eV, respectively.

Table 1. Summary of fitted parameters obtained from time resolved photoluminescence plots shown in figure 6(b) for conventional g-C$_3$N$_4$, pristine CNF-Cl and BiOI/CNF-Cl composites.

Photocatalyst	τ_1 (ns)/A_1	τ_2 (ns)/A_2	τ_3 (ns)/A_3	Average lifetime τ (ns)	Reduced χ^2	Adj. R^2
g-C$_3$N$_4$	0.715/0.765	3.097/0.321	14.827/0.059	8.84	1.91×10^{-5}	0.999
CNF-Cl	2.117/0.780	12.960/0.194	61.726/0.023	23.06	2.90×10^{-7}	0.999
10% BiOI/CNF-Cl	0.072/0.467	3.880/0.398	20.832/0.129	14.53	2.67×10^{-6}	0.999
25% BiOI/CNF-Cl	0.153/0.441	2.867/0.441	16.626/0.114	10.89	7.75×10^{-7}	0.999
50% BiOI/CNF-Cl		1.829/0.776	12.960/0.137	8.02	1.46×10^{-6}	0.999
75% BiOI/CNF-Cl		1.934/0.801	12.900/0.150	8.02	5.40×10^{-7}	0.999

The observed bandgap of g-C$_3$N$_4$ was slightly lower than reported value for bulk g-C$_3$N$_4$ (2.7 eV) which might be due to the use of dicyandiamide precursor instead of melamine and programmed annealing which also affects the degree of polymerization and stacking pattern modifying the bandgap [62–65]. The reduction in the bandgap of fluorinated carbon nitride, compared to g-C$_3$N$_4$ was attributed to the successful doping of F into the C−N matrix, in contrast to counterion-bounded F [22]. The pristine BiOI and BiOI/CNF-Cl composites demonstrate almost similar bandgap (∼1.88 eV) suggesting major absorption was dominated by BiOI. These bandgap values clearly indicate the superior light absorption capabilities of the nanocomposite heterostructures, compared to pristine CNF-Cl.

SSPL spectra of the investigated pristine and composite materials are presented in figure 4(c). CNF-Cl shows an intense and broad SSPL peak centered at ∼500 nm, indicative of a fast band-to-band radiative recombination process of photogenerated electrons and holes. The emission peak of CNF-Cl was red-shifted by ca. 50 nm from the emission peak of bulk g-C$_3$N$_4$, and is similar to the absorption shift seen in figure 4(c). The ∼50 nm redshifts in both the absorption and emission spectra clearly demonstrate the distinct optoelectronic properties of CNF-Cl in comparison to g-C$_3$N$_4$. The SSPL signals for BiOI/CNF-Cl heterostructures were quenched significantly compared to the pristine CNF-Cl, suggesting efficient charge transfer between BiOI and CNF-Cl. These results were similar to the previously reported works of nanocomposite systems comprising BiOI and g-C$_3$N$_4$ [44, 45]. Notice that a significant blue-shift can be observed in the emission spectra of the nanocomposites, relative to pristine CNF-Cl. While no conclusive reason has been identified, electronic interactions between CNF-Cl and BiOI might be responsible for this shift through affecting the relative strength of the $\pi \rightarrow \pi^*$ and $n \rightarrow \pi^*$ transitions in the composite heterostructures. Time resolved photoluminescence (TRPL) spectra were collected (figure 4(d)), and fitted to a tri-exponential decay function of the form:

$$I(t) = A_1 e^{-t/\tau 1} + A_2 e^{-t/\tau 2} + A_3 e^{-t/\tau 3}, \qquad (1)$$

where A_1, A_2 and A_3 represent normalized percentage of each decay components and τ_1, τ_2 and τ_3 are the lifetimes of each decay component, respectively. The presence of three lifetime decay components in most of the fitted curves, is in accord with previously reported TRPL data for carbon nitride-based materials [66, 67]. Table 1 shows the lifetime

decay constants, average lifetime and curve-fitting parameters for conventional g-C$_3$N$_4$, pristine CNF-Cl and BiOI/CNF-Cl nanocomposites. The longest lifetime component in the emission decay g-C$_3$N$_4$ (14.83 ns in table 1) was extended to 61.73 ns in CNF-Cl together with a strong enhancement of its relative intensity, which provides definitive evidence for the suppression of non-radiative recombination pathways due to chlorine intercalation-mediated increased separation between adjacent stacked sheets. The PL decay data taken together with the UV–vis and steady state PL spectra provides further evidence for the distinct optoelectronic properties of CNF-Cl in comparison to bulk g-C$_3$N$_4$.

The carbon nitride framework is constituted of tri-*s*-triazine (heptazine; C$_6$N$_7$) units where sp^2 hybridized carbon and nitrogen overlap together to give σ and π bonding and σ^* and π^* antibonding molecular orbitals. Nonbonded LP electrons on the secondary nitrogens (C–N=C) also contribute to the delocalized π system which promotes formation of an intermediate energy LP-π hybridized π molecular orbital (LP-π hybridized MO) [67–71]. The observed first lifetime decay component for g-C$_3$N$_4$ and CNF-Cl was attributed to direct band-to-band radiative recombination (antibonding $\sigma^* \rightarrow$ LP-π hybridized MO transition and antibonding $\pi^* \rightarrow$ LP-π hybridized MO) while the second decay component arises due to nonradiative relaxation of σ^* electron to π^* orbital followed by radiative recombination with LP-π hybridized MO ($\sigma^* \rightarrow \pi^*$ (non-radiative) and $\pi^* \rightarrow$ LP-π hybridized MO (radiative) [72–74]. The value of the first lifetime and its relative contribution for g-C$_3$N$_4$ was found to be 0.715 ns and 0.765, respectively, while for CNF-Cl, this value was determined to be 2.117 ns and 0.78 ns, respectively. The increased first lifetime of CNF-Cl was attributed to the addition of F atom in heptazine motif breaking the symmetry and transforming some sp^2 hybridized carbons to sp^3 carbon which increases the population of relatively long lived $\sigma^* \rightarrow$ LP-π hybridized MO transitions [22]. The second decay lifetime of CNF-Cl increased to 12.96 ns in comparison to g-C$_3$N$_4$ (3.097 ns) which suggests that the introduction of more electronegative F bonded to sp^3 C in heptazine motif promotes long lived $\sigma^* \rightarrow$ LP-π hybridized MO transition via $\sigma^* \rightarrow \pi^*$ non-radiative relaxation mechanism. Further, decrease in relative contribution (0.194) of the second lifetime of CNF-Cl compared to g-C$_3$N$_4$ (0.321) supports the theory that creation of sp^3 defects via fluorine atom doping reduces the contribution of direct $\pi^* \rightarrow$ LP-π MO recombination due to the reduced conjugation [75, 76]. Interestingly, the third lifetime specific to inter/intra-sheet radiative recombination for
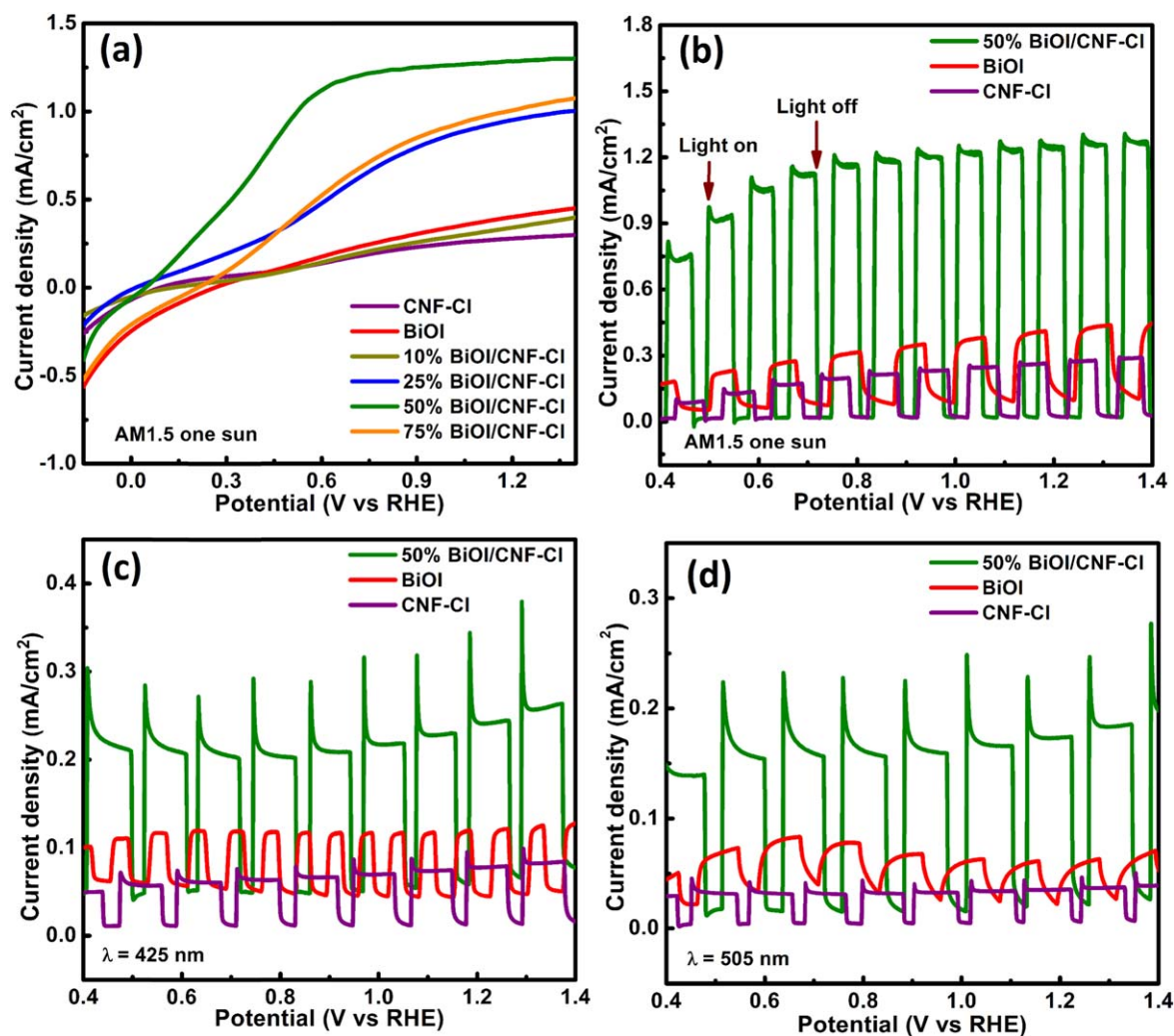
Figure 5. (a) Photocurrent of pristine CNF-Cl, pristine BiOI and BiOI/CNF-Cl composite catalysts under AM1.5 G one sun illumination; (b)–(d) light on–off experiment for pristine CNF-Cl, pristine BiOI and 50% BiOI/CNF-Cl under AM1.5 G one sun illumination, 425 nm (54.15 mW cm^{-2}) and 505 nm (40.48 mW cm^{-2}) LEDs, respectively.

CNF-Cl was found to be 61.726 ns which was much higher than bulk g-C$_3$N$_4$ (14.827 ns). The increased third lifetime suggest better inter-sheets charge migration due to Cl-intercalation which provide interlayer galleries [19]. Further formation of few-layered sheets also facilitate charge separation and reduce recombination resulting in an increased lifetime [66, 67, 77, 78].

The average lifetime (τ_{avg}) is a good metric to quantitatively evaluate the effectiveness of electron–hole separation in the photocatalysts and was determined using the following equation:

$$\tau_{avg} = (A_1\tau_1^2 + A_2\tau_2^2 + A_3\tau_3^2)/ \\ \times (A_1\tau_1 + A_2\tau_2 + A_3\tau_3). \quad (2)$$

The average lifetimes of CNF-Cl, 10% BiOI/CNF-Cl, 25% BiOI/CNF-Cl, 50% BiOI/CNF-Cl, 75% BiOI/CNF-Cl were found to be 23.06, 14.53, 10.89, 8.02 and 8.02 ns, respectively. The lifetimes of both the longest and second-longest PL decay components of CNF-Cl monotonically decreased in the blends with BiOI with the effect saturating at a blend

concentration of 50% and higher. Average lifetimes are significantly reduced for the nanocomposites compared to the pristine CNF-Cl, consistent with the quenching of SSPL intensity discussed earlier in this section. Moreover, the SSPL quenching follows same trend with the TRPL lifetime decay, with the maximum quenching and decay occur for the 50% BiOI/CNF-Cl and 75% BiOI/CNF-Cl heterojunctions. The obtained steady state and transient photoluminescence spectroscopy results suggest better charge separation in the nanocomposites compared to the constituent pristine materials.

2.3. Photoelectrochemical activity test for water splitting

PEC tests were carried out using three electrode system (photocatalyst deposited FTO as anode, Pt cathode and Ag/AgCl reference electrode and Na$_2$SO$_4$). From figure 5(a), it can be seen that the obtained photocurrent density for pristine CNF-Cl was a mere 0.28 mA cm^{-2} at 1.23 V versus RHE (water oxidation potential) which suggests fast intersheet
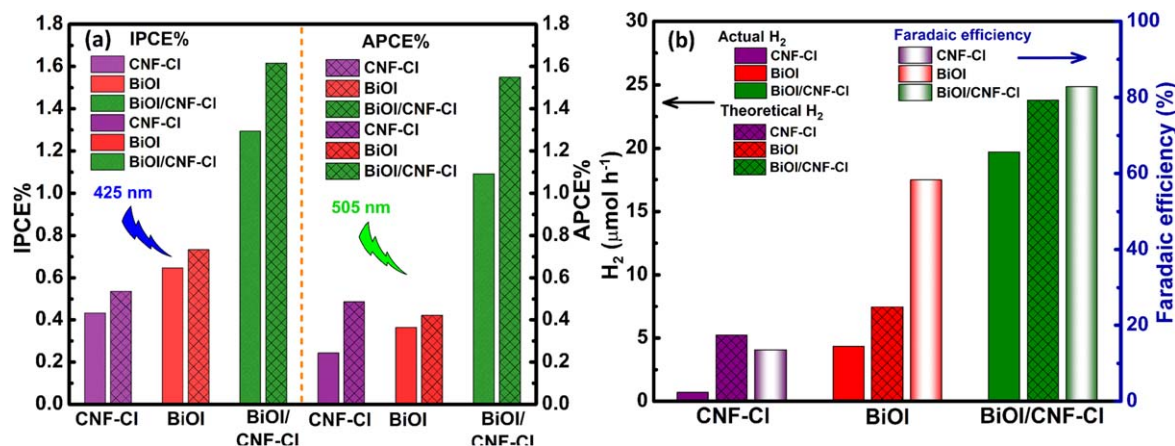
Figure 6. (a) IPCE% and APCE% of CNF-Cl, BiOI and BiOI/CNF-Cl heterojunction. (b) Graph of actually observed H_2 evolution rate determined using GC, theoretically calculated evolution rates from photocurrent and corresponding Faradaic efficiencies.

recombination of photogenerated electron hole pairs. Further, due to a bandgap of 2.05 eV, the CNF-Cl absorbs only the high energy fraction of the visible spectrum to generate electron hole pairs. Similarly, the obtained value of photo-current density for pristine BiOI was found to be a mere 0.40 mA cm^{-2}. However, after formation of heterojunction with CNF-Cl, the photoresponse of the resulting BiOI/CNF-Cl hybrid increased dramatically figure 8(a)). Among various wt% of BiOI (10% BiOI/CNF-Cl, 25% BiOI/CNF-Cl, 50% BiOI/CNF-Cl and 75% BiOI/CNF-Cl) the nanocomposite composed of 50% BiOI and 50% CNF-Cl displayed the highest photocurrent density (1.28 mA cm^{-2}). The photo-current densities for 10% BiOI/CNF-Cl, 25% BiOI/CNF-Cl and 75% BiOI/CNF-Cl heterostructures were measured to be 0.34, 0.95 and 1.01 mA cm^{-2}, respectively. The improved PEC performance of BiOI/CNF-Cl hybrid structure clearly demonstrates improved charge separation due to formation of heterojunction and better charge transport on the surface of conjugated carbon nitride sheets. To validate the true origin of photocurrent and instantaneous photoresponse of materials, photocurrent was measured during light On–Off cycles which clearly displayed rise and drop in photocurrent in On–Off cycles (figure 5(b)).

To discern the PEC performance of the synthesized materials at visible wavelengths, the photocurrent response of materials during On–Off cycles was measured using mono-chromatic 425 nm and 505 nm wavelength LEDs having a power density of 54.15 and 40.48 mW cm^{-2}, respectively, at the surface of photoanode (figures 5(c) and (d)). In compar-ison to pristine CNF-Cl and BiOI, the photocurrent response of heterostructured BiOI/CNF-Cl was much higher which demonstrates synergistic charge separation due to the for-mation of a heterojunction. The photocurrent densities for pristine CNF-Cl, BiOI and heterostructure BiOI/CNF-Cl under 425 nm monochromatic irradiation were obtained to be 0.08, 0.12 and 0.24 mA cm^{-2}, respectively (figure 8(c)). Under 505 nm irradiation the photocurrent densities for CNF-Cl, BiOI and heterostructure BiOI/CNF-Cl were found to be 0.04, 0.06 and 0.18 mA cm^{-2}, respectively (figure 5(d)). 505 nm photons are primarily absorbed by BiOI (see UV–vis

spectra in figure 4(a)). Under illumination by the 505 nm LED, the pristine BiOI photoanode exhibits a slow rise in photocurrent during each On cycle (red curve in figure 5(d)) which is characteristic of the presence of a large number of carrier traps; the photocurrent rises as traps are filled by photogenerated carriers. On the other hand, the BiOI/CNF-Cl photoanode displayed intense spikes instantaneously during light on cycles which decreased and reached a steady state. The spike in photocurrent is due to the instantaneous move-ment of a large number of photogenerated charge carriers because of fast charge separation in the BiOI/CNF-Cl het-erojunction. We attribute the near-exponential decrease in current to reach steady state during each on cycle to trap mediated recombination in BiOI. The EIS Nyquist plot revealed a smaller semicircle arc for the 50% BiOI/CNF-Cl in comparison to pristine films and other blends evidencing a lower charge transfer resistance at semiconductor-electrolyte interface for this composition. Further, the calculated recombination lifetime values were shorter for BiOI/CNFCl heterojunctions suggesting lower resistance for hole transfer to electrolyte and better charge separation within the hetero-structures (see section 4 in the supplementary information, figures S2–S4 and table S1, available online at stacks.iop.org/NANO/31/084001/mmedia). The positive slope in Mott–Schottky plot ($C^{-2}-V$ curves) shows *n*-type conduction of the materials and the calculated flat band positions (V_{FB}) of CNF-Cl, BiOI, 25% BiOI/CNF-Cl, and 50% BiOI/CNF-Cl were calculated to be −0.461, −0.418, −0.521 and −0.675 versus NHE scale at pH-0 (see supplementary data; section 4.0, figures S2 and S4).

The light harvesting performance and efficiency of sub-sequent transformation into electrical energy were calculated from the diagnostic efficiencies under applied bias and irra-diation conditions (figure 6) [79, 80]. The applied bias pho-ton-to-current efficiencies (ABPEs) of pristine CNF-Cl and BiOI were found to be 0.08% and 0.11%, respectively (figure S5 in the supplementary data), while ABPE% of 10% BiOI/CNF-Cl, 25% BiOI/CNF-Cl, 50% BiOI/CNF-Cl and 75% BiOI/CNF-Cl heterostructures were calculated to be 0.09%, 0.31%, 0.71%, and 0.34%, respectively. The maximum

ABPE% was found for 50% BiOI/CNF-Cl which was 8.75 times higher than pristine CNF-Cl and 6.45 times higher than pristine BiOI, respectively. The incident photon-to-current efficiency (IPCE) or external quantum efficiencies (EQEs) of CNF-Cl, BiOI and 50% BiOI/CNF-Cl were calculated to be 0.43%, 0.64% and 1.29% at 425 nm and 0.24%, 0.36% and 1.09% for 505 nm irradiation (figure 5(a)). Furthermore, absorbed photon-to-current efficiency (APCE) or internal quantum efficiency for CNF-Cl, BiOI and BiOI/CNF-Cl under 425 nm irradiation was calculated to be 0.53, 0.73 and 1.61 while under 505 nm these values was found 0.49%, 0.42% and 1.54%, respectively (figure 6(a)). The similarity of the EQE and APCE values merely confirms almost complete light harvesting at 425 and 505 nm wavelengths due to the strong visible absorption of the BiOI/CNF-Cl composites. The EQE values measured under 425 and 505 nm LED illumination are low despite excellent photon harvesting (figure 4(a)), superior charge separation (figures 4(c), (d) and S2–S4) and enhanced recombination suppression (section 2.5) in the BiOI/CNF-Cl heterojunctions. We attribute the low PEC quantum yields to the large exciting binding energy (E_b) of 0.20–0.35 eV (~10 times thermal energy at room temperature) in heptazine motif carbon nitrides [81, 82]. As previously mentioned, fluorination of carbon nitride introduces structural distortions that reduce the conjugation length and further increase E_b [83]. The large values of E_b mean that only a small fraction of the photogenerated excitons are dissociated into free carriers.

2.4. Photoelectrochemical H$_2$ evolution measurement

A three-electrode H-cell containing the deposited materials as the photoanode, Pt cathode and Ag/AgCl reference electrode was used for the measurement of evolved H$_2$ (figure S6). The evolved hydrogen at the Pt counter electrode was analyzed using a gas chromatograph equipped with a pulse discharge ionization detector (figure S7). The observed H$_2$ evolution rates using CNF-Cl, BiOI and BiOI/CNF-Cl as a photoelectrocatalyst were found to be 0.71, 4.35 and 19.71 μmol h^{-1}, respectively. The theoretical H$_2$ evolution rates, based on photocurrent densities for CNF-Cl, BiOI and BiOI/CNF-Cl were calculated to be 5.22, 7.46 and 23.80 μmol h^{-1}, respectively. From these values, the Faradaic efficiencies for CNF-Cl, BiOI and BiOI/CNF-Cl were calculated to be 13.51, 58.29 and 82.83 (percent), respectively (figure 6(b) and table 2). Water splitting occurs at higher applied bias which also promotes side reaction. In such conditions, due to lower reduction potential of SO_4^{2-} ions (+0.172 V versus NHE at pH-0) of Na$_2$SO$_4$, it competes with proton reduction resulting in poor Faradaic efficiency. PEC performance and subsequent characterization of reused BiOI/CNF-Cl showed almost identical photoactivity and structural features as freshly prepared materials, indicating demonstrate resilience and durability of the materials (see supplementary data; section 5.0 figures S8–S10).

Table 2. Photoelectrochemical H$_2$ evolution rate determined experimentally using GC, theoretically calculated evolution rates from photocurrent, and corresponding Faradaic efficiencies.

| Sample	Experimentally evolved H$_2$ (μmol h^{-1} cm^{-2})	Theoretically calculated H$_2$ (μmol h^{-1} cm^{-2})	Faradaic efficiency (%)
CNF-Cl	0.71	5.22	13.51
BiOI	4.35	7.46	58.29
BiOI/CNF-Cl	19.71	23.80	82.83

2.5. Photo-Kelvin probe force microscopy (KPFM)

KPFM has been used for simultaneous structural and electronic property mapping of photovoltaic and photocatalytic materials [84, 85]. Herein, we performed KPFM to image carrier photogeneration (figure 7). Surface potential, which is the difference between contact potentials of the tip and semiconductor surface, was determined both in the dark and under illumination (425 nm LED). The difference between these two surface potentials can be termed as the surface photopotential. Upon illumination, the quasi-Fermi level of a *n*-type semiconductor rises (w.r.t E_{vac}) and thus the difference between the tip work function and semiconductor surface work function increases, compared to the difference in dark condition.

By observing the surface photopotential of different semiconductors, we can quantitatively analyze the photogenerated charge carriers and study the comparative photoresponse. KPFM data was acquired for pristine CNF-Cl, pristine BiOI and 50% BiOI/CNF-Cl. Surface topographic images, surface potential maps and surface potential distributions for all the photocatalysts are shown in figure 7. Dark and illumination conditions are clearly visible in the surface potential mapping and distribution plots. The comparative analysis shows that the nanocomposite photocatalyst 50% BiOI/CNF-Cl has the largest surface photopotential of 207 mV, while pristine CNF-Cl and BiOI have surface photopotential values of 83 mV and 98 mV, respectively. These KPFM data indicates the highest charge carrier (electron) separation occurs in BiOI/CNF-Cl heterostructure compared to the pristine materials. The order of the negative shift of surface potentials for these three materials nicely correlates with their obtained photocurrents ((figure 8). Therefore, the KPFM data corroborates the view of enhanced charge separation in the heterostructured photocatalyst, discussed earlier.

2.6. Photoresponse enhancement mechanism

To explain the improved photocatalytic performance a plausible mechanism was proposed based on electronic band structure and existing literature (figure 8) [46, 86–88]. The process of overall water splitting includes two half reactions (1) hydrogen evolution reaction at the cathode by reduction of protons to hydrogen and (2) oxygen evolution reaction by oxidation of water to oxygen at anode. To achieve efficient
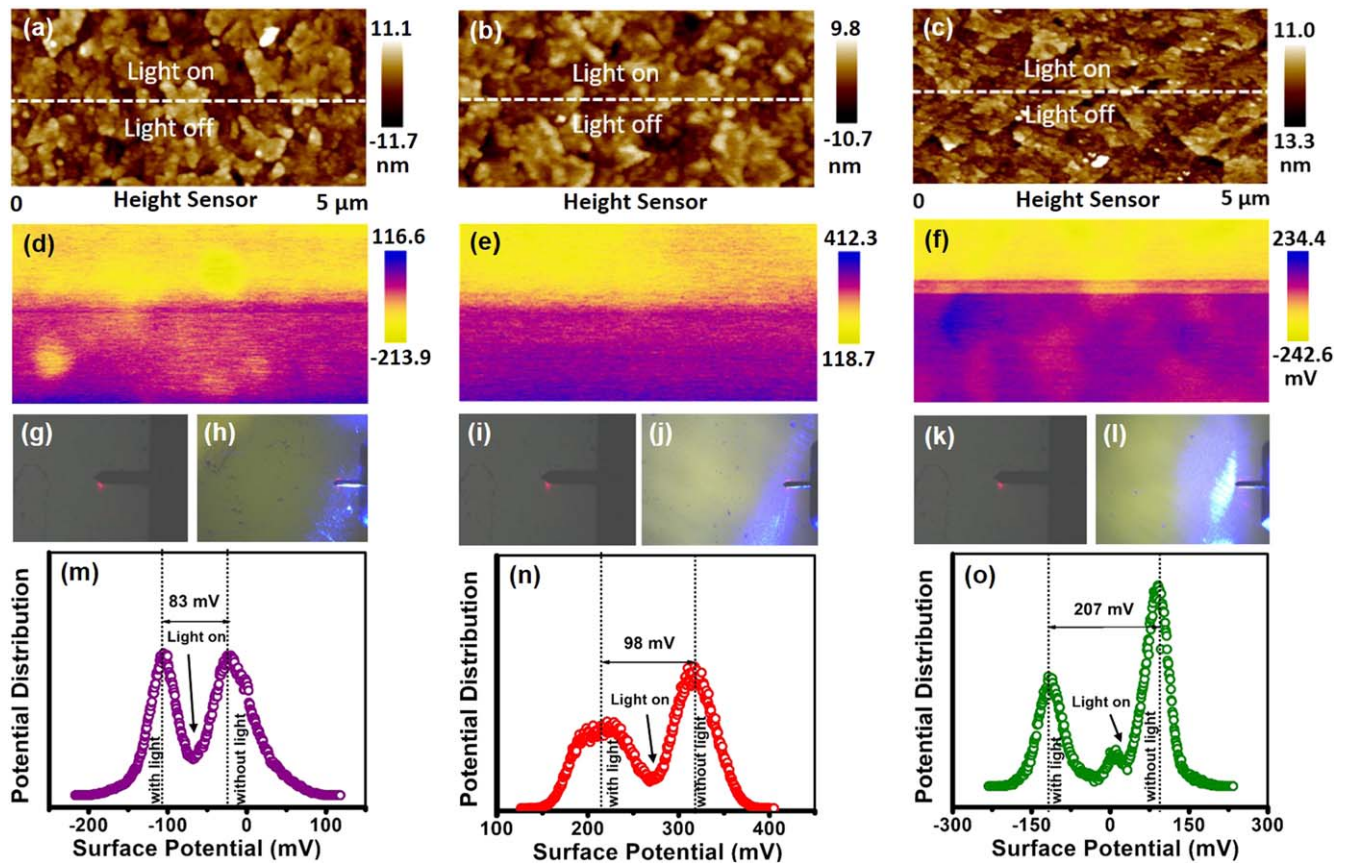
Figure 7. (a)–(c) Surface topographic AFM images of pristine CNF-Cl, pristine BiOI and 50% BiOI/CNF-Cl, respectively; (d)–(f) KPFM surface potential mappings under light (LED 425 nm) (yellow region) and in the dark (purple region) of the samples corresponding to (a)–(c); (g), (i) and (k) AFM tip scan in dark and (h), (j) and (l) AFM tip scan under light (425 nm LED) for the samples corresponding to (a)–(c); (m)–(o) surface potential distribution in the dark and under illumination condition (LED 425 nm) for pristine CNF-Cl, pristine BiOI and 50% BiOI/CNF-Cl, respectively.
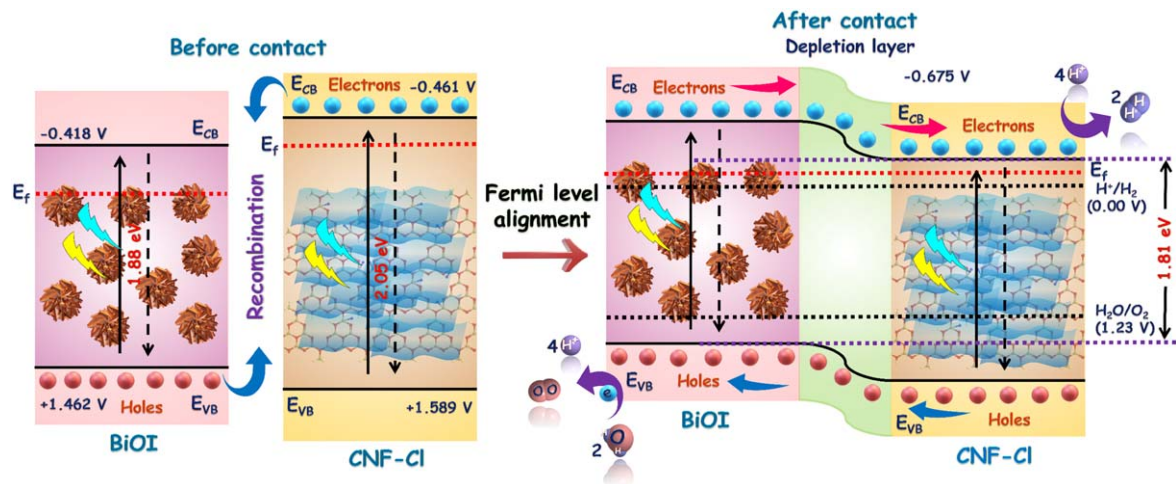
Figure 8. Proposed mechanism of charge separation in BiOI/CNF-Cl composite photoanodes.

water splitting, the conduction band (E_{CB}) position of the semiconductor should be more negative than 0.00 eV versus NHE (reduction potential of proton, H^+/H_2) and valence band (E_{VB}) should be more positive than $+1.23$ eV versus NHE (oxidation potential of water (H_2O/O_2). These requirements suggest that the bandgap of materials should be higher than 1.23 eV [14, 83, 89]. However, wide bandgap

compromises visible light absorption and results in a poor light harvesting efficiency. The optical bandgap of CNF-Cl was found to be 2.05 eV and the E_{CB} and E_{VB} positions were calculated to be -0.461 and $+1.589$ V versus NHE. For BiOI, the bandgap value was 1.82 eV and respective conduction (E_{CB}) and valence (E_{VB}) band positions was found to be -0.418 and $+1.402$ V versus NHE. The bandgaps and

band edge positions of CNF-Cl and BiOI demonstrate that both materials individually fulfill the requirement of water splitting. However, observed photocurrents for pristine CNF-Cl and BiOI were extremely low which can be explained by fast band-to-band charge recombination in BiOI and inter-layer charge recombination in CNF-Cl. After the formation of heterojunction between BiOI and CNF-Cl, the PEC performance of BiOI/CNF-Cl was dramatically enhanced. The improved PEC performance of BiOI/CNF-Cl nanostructures can be explained on the basis of Fermi level alignment which leads to formation of a Type II (staggered) *n*–*n* heterojunction between BiOI and CNF-Cl [90–92]. CNF-Cl displayed strong *n*-type characteristics in Mott Schottky measurement which implies its Fermi level lies just below the conduction band. BiOI displayed weak *n*-type character implying an intermediate position of Fermi level between E_{CB} and E_{VB}. Heterostructure formation of BiOI with CNF-Cl aligns the Fermi levels in the two materials, and is accompanied by a built-in field at the interface between the two semiconductors [93]. During Fermi level alignment, the conduction band of BiOI bends downward while conduction band of CNF-Cl experiences upward band bending as depicted in figure 8 [94].

3. Conclusion

We have demonstrated the synthesis of few-layered fluorine-doped and chlorine-intercalated carbon nitride nanosheets (CNF-Cl) with a reduced bandgap. CNF-Cl also exhibits a red-shifted emission spectrum and substantially longer PL lifetime components in comparison to g-C₃N₄. The likely origin of these lifetime components in the emission decays of g-C₃N₄ and CNF-Cl were explained. These newly synthesized F-doped and Cl-intercalated carbon nitride nanosheets were used to develop heterostructured photocatalysts with earth abundant BiOI. BiOI was found to exhibit weak *n*-type conduction while CNF-Cl was found to be a strongly *n*-type semiconductor. A broad swathe of characterization data including steady state and time-resolved PL spectra, Mott–Schottky plots. KPFM data and photoelectrochemical *J–V* curves are consistent with enhanced charge separation in BiOI/CNF-Cl hybrids due to the formation of a type-II *n*–*n* heterojunction. The enhanced charge separation and extended light harvesting (band-edge of 680 nm) results in significantly increased photoelectrochemical performance compared to the stand-alone constituent materials with photocurrent densities as high as $1.28 \, \text{mA cm}^{-2}$ observed under AM1.5 G one sun illumination. The energy conversion efficiency metric known as ABPE% for the top performing heterojunction (50% BiOI/CNF-Cl) was 8.75 times higher than pristine CNF-Cl and 6.45 times higher than pristine BiOI. Reusability tests and characterization of used photoanodes demonstrated the required robustness and are indicative of long-term operational stability. Furthermore, unusual electronic interactions between BiOI and CNF-Cl were observed that manifested as a significant blue-shift in the steady-state emission spectra of the BiOI/CNF-Cl heterostructures but with little or no effect in the absorption spectra.

ORCID iDs

Pawan Kumar ⓘ https://orcid.org/0000-0003-2804-9298
Karthik Shankar ⓘ https://orcid.org/0000-0001-7347-3333

References

[1] Tachibana Y, Vayssieres L and Durrant J R 2012 Artificial photosynthesis for solar water-splitting *Nat. Photon.* **6** 511
[2] Zheng Y, Lin L, Wang B and Wang X 2015 Graphitic carbon nitride polymers toward sustainable photoredox catalysis *Angew. Chem., Int. Ed.* **54** 12868–84
[3] Wen J, Xie J, Chen X and Li X 2017 A review on g-C₃N₄-based photocatalysts *Appl. Surf. Sci.* **391** 72–123
[4] Wang Q, Hisatomi T, Jia Q, Tokudome H, Zhong M, Wang C, Pan Z, Takata T, Nakabayashi M and Shibata N 2016 Scalable water splitting on particulate photocatalyst sheets with a solar-to-hydrogen energy conversion efficiency exceeding 1% *Nat. Mater.* **15** 611
[5] Wen J, Xie J, Chen X and Li X 2017 A review on g-C₃N₄-based photocatalysts *Appl. Surf. Sci.* **391** 72–123
[6] Naseri A, Samadi M, Pourjavadi A, Moshfegh A Z and Ramakrishna S 2017 Graphitic carbon nitride (gC₃N4)-based photocatalysts for solar hydrogen generation: recent advances and future development directions *J. Mater. Chem.* A **5** 23406–33
[7] Wang X, Maeda K, Thomas A, Takanabe K, Xin G, Carlsson J M, Domen K and Antonietti M 2009 A metal-free polymeric photocatalyst for hydrogen production from water under visible light *Nat. Mater.* **8** 76
[8] Lin Q, Li L, Liang S, Liu M, Bi J and Wu L 2015 Efficient synthesis of monolayer carbon nitride 2D nanosheet with tunable concentration and enhanced visible-light photocatalytic activities *Appl. Catal.* B **163** 135–42
[9] Yin S, Han J, Zhou T and Xu R 2015 Recent progress in gC₃N₄ based low cost photocatalytic system: activity enhancement and emerging applications *Catal. Sci. Technol.* **5** 5048–61
[10] Rajender G, Choudhury B and Giri P 2017 *In situ* decoration of plasmonic Au nanoparticles on graphene quantum dots-graphitic carbon nitride hybrid and evaluation of its visible light photocatalytic performance *Nanotechnology* **28** 395703
[11] Choudhury B 2019 *Nanophotocatalysis and Environmental Applications* (Berlin: Springer) pp 167–209
[12] Ong W-J, Tan L-L, Ng Y H, Yong S-T and Chai S-P 2016 Graphitic carbon nitride (g-C₃N₄)-based photocatalysts for artificial photosynthesis and environmental remediation: are we a step closer to achieving sustainability? *Chem. Rev.* **116** 7159–329

[13] Thomas A, Fischer A, Goettmann F, Antonietti M, Müller J-O, Schlögl R and Carlsson J M 2008 Graphitic carbon nitride materials: variation of structure and morphology and their use as metal-free catalysts *J. Mater. Chem.* **18** 4893–908

[14] Kumar P, Boukherroub R and Shankar K 2018 Sunlight-driven water-splitting using two-dimensional carbon based semiconductors *J. Mater. Chem.* A **6** 12876–931

[15] Kumar P, Vahidzadeh E, Thakur U K, Kar P, Alam K M, Goswami A, Mahdi N, Cui K, Bernard G M and Michaelis V K 2019 C₃N₅: a low bandgap semiconductor containing an Azo-linked carbon nitride framework for photocatalytic, photovoltaic and adsorbent applications *J. Am. Chem. Soc.* **141** 5415–36

[16] Jiang L, Yuan X, Pan Y, Liang J, Zeng G, Wu Z and Wang H 2017 Doping of graphitic carbon nitride for photocatalysis: a reveiw *Appl. Catal.* B **217** 388–406

[17] Zhang G, Zhang M, Ye X, Qiu X, Lin S and Wang X 2014 Iodine modified carbon nitride semiconductors as visible light photocatalysts for hydrogen evolution *Adv. Mater.* **26** 805–9

[18] Wang Y, Li H, Yao J, Wang X and Antonietti M 2011 Synthesis of boron doped polymeric carbon nitride solids and their use as metal-free catalysts for aliphatic C–H bond oxidation *Chem. Sci.* **2** 446–50

[19] Liu C, Zhang Y, Dong F, Reshak A, Ye L, Pinna N, Zeng C, Zhang T and Huang H 2017 Chlorine intercalation in graphitic carbon nitride for efficient photocatalysis *Appl. Catal.* B **203** 465–74

[20] Mane G P, Talapaneni S N, Lakhi K S, Ilbeygi H, Ravon U, Al-Bahily K, Mori T, Park D H and Vinu A 2017 Highly ordered nitrogen-rich mesoporous carbon nitrides and their superior performance for sensing and photocatalytic hydrogen generation *Angew. Chem., Int. Ed.* **56** 8481–5

[21] Ran J, Ma T Y, Gao G, Du X-W and Qiao S Z 2015 Porous P-doped graphitic carbon nitride nanosheets for synergistically enhanced visible-light photocatalytic H₂ production *Energy Environ. Sci.* **8** 3708–17

[22] Wang Y, Di Y, Antonietti M, Li H, Chen X and Wang X 2010 Excellent visible-light photocatalysis of fluorinated polymeric carbon nitride solids *Chem. Mater.* **22** 5119–21

[23] Yang S, Gong Y, Zhang J, Zhan L, Ma L, Fang Z, Vajtai R, Wang X and Ajayan P M 2013 Exfoliated graphitic carbon nitride nanosheets as efficient catalysts for hydrogen evolution under visible light *Adv. Mater.* **25** 2452–6

[24] Schwinghammer K, Mesch M B, Duppel V, Ziegler C, Senker J R and Lotsch B V 2014 Crystalline carbon nitride nanosheets for improved visible-light hydrogen evolution *J. Am. Chem. Soc.* **136** 1730–3

[25] Ou H, Lin L, Zheng Y, Yang P, Fang Y and Wang X 2017 Tri-s-triazine-based crystalline carbon nitride nanosheets for an improved hydrogen evolution *Adv. Mater.* **29** 1700008

[26] Zhang J, Chen Y and Wang X 2015 Two-dimensional covalent carbon nitride nanosheets: synthesis, functionalization, and applications *Energy Environ. Sci.* **8** 3092–108

[27] Zhang X, Xie X, Wang H, Zhang J, Pan B and Xie Y 2012 Enhanced photoresponsive ultrathin graphitic-phase C₃N₄ nanosheets for bioimaging *J. Am. Chem. Soc.* **135** 18–21

[28] Xu J, Zhang L, Shi R and Zhu Y 2013 Chemical exfoliation of graphitic carbon nitride for efficient heterogeneous photocatalysis *J. Mater. Chem.* A **1** 14766–72

[29] She X, Xu H, Xu Y, Yan J, Xia J, Xu L, Song Y, Jiang Y, Zhang Q and Li H 2014 Exfoliated graphene-like carbon nitride in organic solvents: enhanced photocatalytic activity and highly selective and sensitive sensor for the detection of trace amounts of Cu₂ *J. Mater. Chem.* A **2** 2563–70

[30] Lu X, Xu K, Chen P, Jia K, Liu S and Wu C 2014 Facile one step method realizing scalable production of gC₃N₄ nanosheets and study of their photocatalytic H₂ evolution activity *J. Mater. Chem.* A **2** 18924–8

[31] Wu M, Yan J M, Tang X N, Zhao M and Jiang Q 2014 Synthesis of potassium-modified graphitic carbon nitride with high photocatalytic activity for hydrogen evolution *ChemSusChem* **7** 2654–8

[32] Bhachu D S, Moniz S J, Sathasivam S, Scanlon D O, Walsh A, Bawaked S M, Mokhtar M, Obaid A Y, Parkin I P and Tang J 2016 Bismuth oxyhalides: synthesis, structure and photoelectrochemical activity *Chem. Sci.* **7** 4832–41

[33] Cheng H, Huang B and Dai Y 2014 Engineering BiOX (X = Cl, Br, I) nanostructures for highly efficient photocatalytic applications *Nanoscale* **6** 2009–26

[34] Guan M, Xiao C, Zhang J, Fan S, An R, Cheng Q, Xie J, Zhou M, Ye B and Xie Y 2013 Vacancy associates promoting solar-driven photocatalytic activity of ultrathin bismuth oxychloride nanosheets *J. Am. Chem. Soc.* **135** 10411–7

[35] Zhang X, Ai Z, Jia F and Zhang L 2008 Generalized one-pot synthesis, characterization, and photocatalytic activity of hierarchical BiOX (X = Cl, Br, I) nanoplate microspheres *J. Phys. Chem.* C **112** 747–53

[36] Meng X and Zhang Z 2018 New insight into BiOX (X = Cl, Br, and I) hierarchical microspheres in photocatalysis *Mater. Lett.* **225** 152–6

[37] Liu Q-C, Ma D-K, Hu Y-Y, Zeng Y-W and Huang S-M 2013 Various bismuth oxyiodide hierarchical architectures: alcohothermal-controlled synthesis, photocatalytic activities, and adsorption capabilities for phosphate in water *ACS Appl. Mater. Interfaces* **5** 11927–34

[38] Huang Y, Li H, Balogun M-S, Liu W, Tong Y, Lu X and Ji H 2014 Oxygen vacancy induced bismuth oxyiodide with remarkably increased visible-light absorption and superior photocatalytic performance *ACS Appl. Mater. Interfaces* **6** 22920–7

[39] Mera A C, Moreno Y, Pivan J-Y, Peña O and Mansilla H D 2014 Solvothermal synthesis of BiOI microspheres: effect of the reaction time on the morphology and photocatalytic activity *J. Photochem. Photobiol.* A **289** 7–13

[40] Gan J, Rajeeva B B, Wu Z, Penley D and Zheng Y 2016 Hydrogen-reduced bismuth oxyiodide nanoflake arrays with plasmonic enhancements for efficient photoelectrochemical water reduction *Electrochim. Acta* **219** 20–7

[41] Su J, Xiao Y and Ren M 2014 Direct hydrolysis synthesis of BiOI flowerlike hierarchical structures and it's photocatalytic activity under simulated sunlight irradiation *Catal. Commun.* **45** 30–3

[42] An H, Lin B, Xue C, Yan X, Dai Y, Wei J and Yang G 2018 Formation of BiOI/g-C₃N₄ nanosheet composites with high visible-light-driven photocatalytic activity *Chin. J. Catal.* **39** 654–63

[43] Wang J-C, Yao H-C, Fan Z-Y, Zhang L, Wang J-S, Zang S-Q and Li Z-J 2016 Indirect Z-scheme BiOI/g-C₃N₄ photocatalysts with enhanced photoreduction CO₂ activity under visible light irradiation *ACS Appl. Mater. Interfaces* **8** 3765–75

[44] Chou S-Y, Chen C-C, Dai Y-M, Lin J-H and Lee W W 2016 Novel synthesis of bismuth oxyiodide/graphitic carbon nitride nanocomposites with enhanced visible-light photocatalytic activity *RSC Adv.* **6** 33478–91

[45] Di J, Xia J, Yin S, Xu H, Xu L, Xu Y, He M and Li H 2014 Preparation of sphere-like gC₃N₄/BiOI photocatalysts via a reactable ionic liquid for visible-light-driven photocatalytic degradation of pollutants *J. Mater. Chem.* A **2** 5340–51

[46] Chang C, Zhu L, Wang S, Chu X and Yue L 2014 Novel mesoporous graphite carbon nitride/BiOI heterojunction for enhancing photocatalytic performance under visible-light irradiation *ACS Appl. Mater. Interfaces* **6** 5083–93

[47] Alam K M, Kumar P, Kar P, Thakur U K, Zeng S, Cui K and Shankar K 2019 Enhanced charge separation in g-C₃N₄–BiOI heterostructures for visible light driven

photoelectrochemical water splitting *Nanoscale Adv.* **1** 1460–71

[48] Liu B, Han X, Wang Y, Fan X, Wang Z, Zhang J and Shi H 2018 Synthesis of gC$_3$N$_4$/BiOI/BiOBr heterostructures for efficient visible-light-induced photocatalytic and antibacterial activity *J. Mater. Sci., Mater. Electron.* **29** 14300–10

[49] Meng X, Jiang L, Wang W and Zhang Z 2015 Enhanced photocatalytic activity of BiOBr/ZnO heterojunction semiconductors prepared by facile hydrothermal method *Int. J. Photoenergy* **2015**

[50] Pan C, Xu J, Wang Y, Li D and Zhu Y 2012 Dramatic activity of C$_3$N$_4$/BiPO$_4$ photocatalyst with core/shell structure formed by self-assembly *Adv. Funct. Mater.* **22** 1518–24

[51] Peng H, Chan C K, Meister S, Zhang X F and Cui Y 2008 Shape evolution of layer-structured bismuth oxychloride nanostructures via low-temperature chemical vapor transport *Chem. Mater.* **21** 247–52

[52] Liu J, Zhang T, Wang Z, Dawson G and Chen W 2011 Simple pyrolysis of urea into graphitic carbon nitride with recyclable adsorption and photocatalytic activity *J. Mater. Chem.* **21** 14398–401

[53] Yuan S, Rösner M, Schulz A, Wehling T O and Katsnelson M I 2015 Electronic structures and optical properties of partially and fully fluorinated graphene *Phys. Rev. Lett.* **114** 047403

[54] Luo S, Xu J, Li Z, Liu C, Chen J, Min X, Fang M and Huang Z 2017 Bismuth oxyiodide coupled with bismuth nanodots for enhanced photocatalytic bisphenol A degradation: synergistic effects and mechanistic insight *Nanoscale* **9** 15484–93

[55] Ferrari A C and Robertson J 2000 Interpretation of Raman spectra of disordered and amorphous carbon *Phys. Rev.* B **61** 14095

[56] Dresselhaus M S, Jorio A, Hofmann M, Dresselhaus G and Saito R 2010 Perspectives on carbon nanotubes and graphene Raman spectroscopy *Nano Lett.* **10** 751–8

[57] Wang H, Zhang X, Xie J, Zhang J, Ma P, Pan B and Xie Y 2015 Structural distortion in graphitic-C$_3$N$_4$ realizing an efficient photoreactivity *Nanoscale* **7** 5152–6

[58] Chowdhury A, Cameron D and Hashmi M 1998 Vibrational properties of carbon nitride films by Raman spectroscopy *Thin Solid Films* **332** 62–8

[59] Bankar P K, Warule S S, Jadkar S R, Chaudhari N S and More M A 2016 Nanostructured BiOI–GO composite: facile room temperature synthesis with enhanced multifunctionality in field emission and photocatalytic activity *RSC Adv.* **6** 83084–90

[60] Kumar A, Kumar P, Joshi C, Ponnada S, Pathak A K, Ali A, Sreedhar B and Jain S L 2016 A [Fe (bpy) 3] 2 + grafted graphitic carbon nitride hybrid for visible light assisted oxidative coupling of benzylamines under mild reaction conditions *Green Chem.* **18** 2514–21

[61] Jorge A B, Martin D J, Dhanoa M T, Rahman A S, Makwana N, Tang J, Sella A, Corà F, Firth S and Darr J A 2013 H$_2$ and O$_2$ evolution from water half-splitting reactions by graphitic carbon nitride materials *J. Phys. Chem.* C **117** 7178–85

[62] Hang L T, Lai N D, Phuong N T, Thang D V, Hung N M and Van Minh N 2018 Influence of annealing temperature on physical properties and photocatalytic ability of g-C$_3$N$_4$ nanosheets synthesized through urea polymerization in Ar atmosphere *Physica* B **532** 48–53

[63] Zhang W, Zhang Q, Dong F and Zhao Z 2013 The multiple effects of precursors on the properties of polymeric carbon nitride *Int. J. Photoenergy* **2013** 685038

[64] Martin D J, Qiu K, Shevlin S A, Handoko A D, Chen X, Guo Z and Tang J 2014 Highly efficient photocatalytic H$_2$ evolution from water using visible light and structure-controlled graphitic carbon nitride *Angew. Chem., Int. Ed.* **53** 9240–5

[65] Dong G and Zhang L 2012 Porous structure dependent photoreactivity of graphitic carbon nitride under visible light *J. Mater. Chem.* **22** 1160–6

[66] Yang P, Ou H, Fang Y and Wang X 2017 A facile steam reforming strategy to delaminate layered carbon nitride semiconductors for photoredox catalysis *Angew. Chem., Int. Ed.* **56** 3992–6

[67] Zhang Y, Pan Q, Chai G, Liang M, Dong G, Zhang Q and Qiu J 2013 Synthesis and luminescence mechanism of multicolor-emitting gC$_3$N$_4$ nanopowders by low temperature thermal condensation of melamine *Sci. Rep.* **3** 1943

[68] Niu P, Liu G and Cheng H-M 2012 Nitrogen vacancy-promoted photocatalytic activity of graphitic carbon nitride *J. Phys. Chem.* C **116** 11013–8

[69] Shalom M, Inal S, Fettkenhauer C, Neher D and Antonietti M 2013 Improving carbon nitride photocatalysis by supramolecular preorganization of monomers *J. Am. Chem. Soc.* **135** 7118–21

[70] Kang Y, Yang Y, Yin L C, Kang X, Wang L, Liu G and Cheng H M 2016 Selective breaking of hydrogen bonds of layered carbon nitride for visible light photocatalysis *Adv. Mater.* **28** 6471–7

[71] Shi R, Li Z, Yu H, Shang L, Zhou C, Waterhouse G I, Wu L Z and Zhang T 2017 Effect of nitrogen doping level on the performance of N-Doped carbon quantum Dot/TiO$_2$ composites for photocatalytic hydrogen evolution *ChemSusChem* **10** 4650–6

[72] Chen L C, Teng C Y, Lin C Y, Chang H Y, Chen S J and Teng H 2016 Architecting nitrogen functionalities on graphene oxide photocatalysts for boosting hydrogen production in water decomposition process *Adv. Energy Mater.* **6** 1600719

[73] Godin R, Wang Y, Zwijnenburg M A, Tang J and Durrant J R 2017 Time-resolved spectroscopic investigation of charge trapping in carbon nitrides photocatalysts for hydrogen generation *J. Am. Chem. Soc.* **139** 5216–24

[74] Shalom M, Guttentag M, Fettkenhauer C, Inal S, Neher D, Llobet A and Antonietti M 2014 *In situ* formation of heterojunctions in modified graphitic carbon nitride: synthesis and noble metal free photocatalysis *Chem. Mater.* **26** 5812–8

[75] Liang Q, Li Z, Huang Z H, Kang F and Yang Q H 2015 Holey graphitic carbon nitride nanosheets with carbon vacancies for highly improved photocatalytic hydrogen production *Adv. Funct. Mater.* **25** 6885–92

[76] She X, Wu J, Zhong J, Xu H, Yang Y, Vajtai R, Lou J, Liu Y, Du D and Li H 2016 Oxygenated monolayer carbon nitride for excellent photocatalytic hydrogen evolution and external quantum efficiency *Nano Energy* **27** 138–46

[77] Niu P, Zhang L, Liu G and Cheng H M 2012 Graphene-like carbon nitride nanosheets for improved photocatalytic activities *Adv. Funct. Mater.* **22** 4763–70

[78] Meng N, Ren J, Liu Y, Huang Y, Petit T and Zhang B 2018 Engineering oxygen-containing and amino groups into two-dimensional atomically-thin porous polymeric carbon nitrogen for enhanced photocatalytic hydrogen production *Energy Environ. Sci.* **11** 566–71

[79] Varghese O K and Grimes C A 2008 Appropriate strategies for determining the photoconversion efficiency of water photoelectrolysis cells: a review with examples using titania nanotube array photoanodes *Sol. Energy Mater. Sol. Cells* **92** 374–84

[80] Chen Z, Dinh H N and Miller E 2013 *Photoelectrochemical Water Splitting* (Berlin: Springer)

[81] Melissen S, Le Bahers T, Steinmann S N and Sautet P 2015 Relationship between carbon nitride structure and exciton

binding energies: a DFT perspective *J. Phys. Chem.* C **119** 25188–96

[82] Sun J, Li X and Yang J 2018 The roles of buckled geometry and water environment in the excitonic properties of graphitic C3N4 *Nanoscale* **10** 3738–43

[83] Kumar P, Thakur U K, Alam K, Kar P, Kisslinger R, Zeng S, Patel S and Shankar K 2018 Arrays of TiO$_2$ nanorods embedded with fluorine doped carbon nitride quantum dots (CNFQDs) for visible light driven water splitting *Carbon* **137** 174–87

[84] Spadafora E J, Demadrille R, Ratier B and Grévin B 2010 Imaging the carrier photogeneration in nanoscale phase segregated organic heterojunctions by Kelvin probe force microscopy *Nano Lett.* **10** 3337–42

[85] Wu M-C, Liao H-C, Cho Y-C, Tóth G, Chen Y-F, Su W-F and Kordas K 2013 Photo-Kelvin probe force microscopy for photocatalytic performance characterization of single filament of TiO$_2$ nanofiber photocatalysts *J. Mater. Chem.* A **1** 5715–20

[86] Roger I, Shipman M A and Symes M D 2017 Earth-abundant catalysts for electrochemical and photoelectrochemical water splitting *Nat. Rev. Chem.* **1** 0003

[87] Nellist M R, Laskowski F A, Lin F, Mills T J and Boettcher S W 2016 Semiconductor–electrocatalyst interfaces: theory, experiment, and applications in photoelectrochemical water splitting *Acc. Chem. Res.* **49** 733–40

[88] Indra A, Acharjya A, Menezes P W, Merschjann C, Hollmann D, Schwarze M, Aktas M, Friedrich A, Lochbrunner S and Thomas A 2017 Boosting visible-light-driven photocatalytic hydrogen evolution with an integrated nickel phosphide–carbon nitride system *Angew. Chem., Int. Ed.* **56** 1653–7

[89] Hisatomi T, Kubota J and Domen K 2014 Recent advances in semiconductors for photocatalytic and photoelectrochemical water splitting *Chem. Soc. Rev.* **43** 7520–35

[90] Wang Y, Wang Q, Zhan X, Wang F, Safdar M and He J 2013 Visible light driven type II heterostructures and their enhanced photocatalysis properties: a review *Nanoscale* **5** 8326–39

[91] Li H, Zhou Y, Tu W, Ye J and Zou Z 2015 State-of-the-art progress in diverse heterostructured photocatalysts toward promoting photocatalytic performance *Adv. Funct. Mater.* **25** 998–1013

[92] Dashtian K, Ghaedi M, Shirinzadeh H, Hajati S and Shahbazi S 2018 Achieving enhanced blue-light-driven photocatalysis using nanosword-like VO$_2$/CuWO$_4$ type II n–n heterojunction *Chem. Eng. J.* **339** 189–203

[93] Mu J, Miao H, Liu E, Feng J, Teng F, Zhang D, Kou Y, Jin Y, Fan J and Hu X 2018 Enhanced light trapping and high charge transmission capacities of novel structures for efficient photoelectrochemical water splitting *Nanoscale* **10** 11881–93

[94] Afroz K, Moniruddin M, Bakranov N, Kudaibergenov S and Nuraje N 2018 A heterojunction strategy to improve the visible light sensitive water splitting performance of photocatalytic materials *J. Mater. Chem.* A **6** 21696–718